

Supplementary Information for

Simultaneous polymerization and adhesion under hypoxia in sickle cell anemia

Dimitrios P. Papageorgiou, Sabia Z. Abidi, Hung-Yu Chang, Xuejin Li, Gregory J. Kato, George E. Karniadakis, Subra Suresh* and Ming Dao*

*Subra Suresh, E-mail: ssuresh@ntu.edu.sg

*Ming Dao, E-mail: mingdao@mit.edu

This PDF file includes:

- Supplementary text
- Figs. S1 to S7
- Tables S1 to S2
- Captions for Movies S1 to S12
- References for SI reference citations

Other supplementary materials for this manuscript include the following:

- Movies S1 to S12

Supporting Information Text

Blood Specimens

Blood samples were drawn from homozygous SS sickle cell disease patients at the University of Pittsburgh, Pittsburgh, PA (University of Pittsburgh IRB protocol PRO08110422) and the Massachusetts General Hospital, Boston, MA under a protocol of Excess Human Materials approved by the Partners Healthcare IRB with a waiver of consent. On-hydroxyurea treatment and off-hydroxyurea treatment patient samples were used. Sample specimens used for this study were restricted to patients that were not in crisis and patients with transfusions 30 days prior to blood draw. Blood was collected in 4 ml K2 ethylenediaminetetraacetic acid (EDTA) spray-coated anticoagulant vacutainers (1.8 mg/ml). Sample vacutainers were shipped to MIT on melting ice by overnight delivery and stored at 4 °C. Hemoglobin fractions were determined with cellulose agar electrophoresis and confirmed by high performance liquid chromatography. Density gradient centrifugation of the anticoagulated blood was performed at $820 \times g$ for 5 minutes. The buffy coat and blood plasma were removed. The remaining packed red blood cells (pRBC) were then washed twice with centrifugation ($820 \times g$ for 5 minutes each time) with Dulbecco's phosphate buffer saline (HyClone DPBS; Thermo Scientific). The pRBC pellet was resuspended in HyClone DPBS with 1% (w/v) bovine serum albumin (BSA) (EMD Millipore, Billerica, MA) at a concentration of 2-3 μl pRBC per 200 μl of medium solution. pRBC suspensions were stored at 4 °C until use.

Sickle RBC density fractionation

Fractionation of sickle RBCs was performed as described in (1). Briefly, OptiPrep (Sigma-Aldrich) Density Gradient Medium was used to create a stepwise liquid gradient to separate RBCs based on their respective cell density. PBS was used to adjust the OptiPrep medium density as follows: Density 1: 1.086 g/ml; Density 2: 1.095 g/ml; Density 3: 1.105 g/ml, and Density 4: >1.111 g/ml. The different liquid densities were layered in volumes of 2.5-ml within a 15 ml centrifuge tube, starting with the "Density 4" layer placed at the bottom of the tube. The packed RBCs were washed two times with PBS and centrifuged at $820 \times g$ at 21 °C for 5 min. Then the packed RBCs were resuspended in PBS to achieve a 70–80% hematocrit, and layered on top of the least dense layer within the centrifuge tube for centrifugation at $820 \times g$ for 30 min at 21 °C. Following centrifugation, the cell populations fractionated between the density layers were isolated carefully. Following the removal of the gradient OptiPrep medium (two washes with PBS), the fractionated cells were resuspended in PBS with 1% BSA where approximately 1 μl of pellet was suspended in 200 μl of PBS–BSA and kept at 4 °C until use.

All of the microfluidics tests were conducted within 1-3 days following blood draw. Hematology and hemoglobin electrophoresis results for all samples are summarized in [Table S1](#).

Device Fabrication

The assembled microfluidic devices comprised a two-layer straight microchannel structure ("flow" and "gas" channels) separated by a free-standing gas-permeable membrane ([Fig. S1](#)). Each device was fabricated using two different master molds, lithographically patterned with SU-8 negative photoresist (Microchem Corporation, Newton, MA, USA) on a 6-inch silicon wafer. To aid the removal of PDMS from SU-8, all fabricated SU-8 masters were passivated in vacuum for 2 h using fluorosilane vapor: T2492-KG, (tridecafluoro-1,1,2,2-tetrahydrooctyl)-1-trichlorosilane (United Chemical Technologies). Commercial thermocurable PDMS material (Sylgard® 184 silicone elastomer, Dow Corning, Auburn, MI) was used. The prepolymer of PDMS was prepared by mixing the base and the curing agent at a 10:1 weight ratio. Then PDMS prepolymers were either spin-coated (150 μm layer) on the flow-channel SU-8 mold or casted in the gas-channel SU-8 mold (5 mm thick) after vacuum degassing. Thermal crosslinking of PDMS films and slabs was performed by curing at 80°C for 2h in both spin-coated and casted masters. Following thermal curing, the inlet and outlet access ports were punched through the gas channel, with diameter of 1.5 mm (Uni-Core™ punches, Sigma-Aldrich, St. Louis, MO, USA). Then, the flow channel was aligned to the gas channel in a "cross" configuration to create a rectangular gas-exchange region. The two-layer device was then separated from the SU-8 master and the flow layer ports are punched. Then, the two layer stack was bonded to microscope coverslip substrates using air-plasma treatment (Harrick plasma, PDC-001).

Device Functionalization

We deposited (3-aminopropyl)-trimethoxysilane (APTMS) from the gas-phase for 2 h at room temperature on air-plasma-treated PDMS slabs and microscope coverslips (Harrick plasma, PDC-001). After silanization and bonding, the devices were incubated with FITC-conjugated fibronectin (Cytoskeleton, Denver, CO) in PBS (60 $\mu\text{g}/\text{ml}$) for 1 h at room temperature. The devices were then passivated with a 3% (w/v) BSA (EMD Millipore, Billerica, MA) in PBS solution over night at 4°C and used within 24-48 h. The amount of protein on the microchannel walls was ~ 4.5 g/m^2 . FITC fluorescent intensity images of the FN-functionalized channels were acquired using a 10x objective lens to ensure assay reproducibility. Fluorescence intensity was compared using ImageJ (NIH, Bethesda, MD).

Experimental Setup

We designed an *in vitro* microfluidic platform and implemented a pneumatic pump setup that mimics the *in vivo* post-capillary venule (~ 10 - 100 μm in diameter) sickle cell adhesion ([Fig. S1](#)). With the ability to simulate normoxia or hypoxia *i.e.*, low

oxygen partial pressure (pO_2) conditions, we can simultaneously characterize the isolated effects of sickle RBC adhesive dynamics on functionalized surfaces at a single-cell level.

Sickle RBC adhesive dynamics was observed and quantified in a microfluidic device comprising a free-standing gas-permeable polydimethylsiloxane (PDMS) membrane ($\sim 150 \mu\text{m}$ thick) within a dual-layer microchannel construction. Device design is also described in (2) and is optimized in terms of wall functionalization with fibronectin (FN) to study cell adhesion dynamics. A schematic representation of the microfluidic device is shown in Fig. S1. The dual-layer device comprises a "flow microchannel" ($\sim 5 - 15 \mu\text{m}$ depth) in which there was flow of an RBC suspension, and a "gas microchannel" ($100 \mu\text{m}$ depth) in which the desired gas mixture was delivered and the oxygen partial pressure regulated. Both flow and gas channels were 3 mm in length and 1.326 mm in width and laid out in a cross configuration. Both flow and gas channels were connected with in-line pressure and flow rate sensors (with feedback loop). This allowed to precisely control the oxygen level of the RBC's microenvironment as well as the wall shear stress within the devices' region of interest (ROI).

The flow channels' rectangular cross section at the ROI has an equivalent hydraulic diameter range of $D_h \sim 10 - 30 \mu\text{m}$. The shear stress near the walls is within the range of $\tau \sim 0.035 - 0.085 \text{ Pa}$. Within the gas microchannel, pressurized gas is delivered via a high precision pneumatic pump and the O_2 concentration is controlled by exchanging gas flow in the channel through the PDMS membrane as follows: *Normoxia*: O_2 concentration $\sim 20\%$ (vol/vol); *Hypoxia*: O_2 concentration $< 5\%$. This platform can deliver rapid deoxygenation to the RBCs in which the O_2 concentration decreased from 20 vol% to below 5 vol% within 15 s and maintained at 2 vol% for the rest periods. Transient hypoxia profiles via this platform also explained in detail in (2, 3).

Furthermore, to enhance the imaging contrast of RBCs *i.e.*, to isolate the information carried by the Hb at 410 nm and 430 nm, a 414/46-nm single-band bandpass filter was used (Semrock). The morphology of the RBCs in hypoxia was visually enhanced, especially in the case of the sickle reticulocyte population the filter greatly helped the visualization of the HbS fiber projections and subsequent retraction of them under reoxygenation.

Lastly, microfluidic device imaging was performed using Zeiss Axiovert 200 and Olympus IX71 inverted microscopes. Hitachi KP-D20A CCD (752p x 582p,) and Olympus DP72 cameras were used for image acquisition. All testing was performed at 37°C using a heating incubator (ibidi heating system, ibidi USA).

Adherent Sickle Cells

Classification. Following the cell classification models of Mohandas (4–7), Kaul (8), Bessis and Bricka (9) and sickle cell specific classification tools developed in-house (10), we categorized adherent sickle cells into the following categories: (I) sickle reticulocytes (SRs), (II) sickle mature erythrocytes (SMEs) of any shape, and (III) irreversibly-sickled cells (ISCs) (Fig. S2).

SR maturity stages can be further distinguished readily from each other based only on morphological differences: (1) Class 1 sickle reticulocytes (SR1), which are the least mature have a multi-lobular morphology and are relatively motile; and (2) Class 2 more mature sickle reticulocytes (SR2), which are asymmetric "deep dish" morphology, non-motile and feature a highly refractile concentric ring and visible granules (generally one to three in number). The aforementioned classification is identical to the two-stage cell cytological classification for reticulocytes in the rat in (5); where SR1 is the R1 population and SR2 is the R2 population. Regarding the SR1 and the SR2 cell population; the classification criteria in specifying any microscopic classification scheme involves a relative uncertainty or subjectivity of decision. However, as described by Mohandas et al. (5, 6) the reproducibility and precision of the unstained, live cell classification scheme appears at least as good as the one obtained by staining.

In-between SRs and SMEs there is an intermediate reticulocyte maturation stage *i.e.*, the R3s; which have not attained the normal discocyte shape yet and generally represent intermediates between SR2s and mature erythrocytes (4). In our adherence classification scheme we include those cells within the SME subpopulation.

SMEs were further classified based on adherence observations under hypoxia. Two categories were generated according to their shape changes compared to their corresponding normoxia-shape as follows: (I) Class I mature sickle erythrocytes (SME1) which exhibit significant morphological shape change under hypoxia (Fig. S2, SME1s, black background). In normoxia these cells are discoid sickle cells and have smooth surface contours similar to the classification of Mohandas (11) (Fig. S2, SME1s, grey background). Note that in some SME1 image pairs in hypoxia and subsequent reoxygenation there are residual adhesion sites which do not classify as irregular contours. (II) Class II mature sickle cells (SME2) that largely maintain their normoxia-shape in hypoxia (*i.e.*, minimal morphological change) while the cell appears to have irregular surface contours (Fig. S2, SME2s, black background). In normoxia these cells are mostly elliptocytic sickle cells with already slightly irregular surface contours (Fig. S2, SME2s, grey background)

ISCs have elongated and elliptocytic morphology in addition to irregular surface contours in normoxia (Fig. S2, ISCs). Cells classified as "Other" are cells of mostly echinocyte-type and odd-shaped cells that do not fall into any of the previous categories.

Finally, we also classify the unsicklable adherent sickle cells *i.e.*, cells that maintain their normoxia shape throughout our 10 min hypoxic adherence assay.

Statistics. In Fig. S3 cell population statistics are presented. Fig. S3A shows individual non-density-fractionated adherent cell data (% of the total cells per sample) for Patients I, II, III, IV and VIII as identified in Table S1. Fig. S3B shows bundled non-density-fractionated adherent cell data (% of the total cells per sample) for Patients I, II, III, IV and VIII (Table S1). Between SME1s and any other cell category the means difference is significant at the $P < 0.0001$ level, except between SME1s and SME2s where $P < 0.001$ as indicated in the plot.

Fig. S3C shows density-fractionated adherent cell data (% of the total cells) for Patient III (Table S1). It is evident that density fraction 2 comprises predominately of SME1 and unsickable cells (90% of the total combined) whereas in density fraction 4, ISCs and SME2s are mostly adherent (84% of the total combined).

Patient III as well as Patient IV has also been reported in our recent study (1), in which we measured the normoxic biomechanical properties as a function of cell density via membrane fluctuations (identified as Patients V and XI respectively in that study). In that study, statistically significant data were presented of the increase in the membrane shear modulus and surface to volume increase as the cell density increases, which is correlated with average cell deformability. As a result SME1s exhibit higher average deformability than SME2s.

Simulation Model and Method

We have performed computational studies of cell adhesion dynamics based on dissipative particle dynamics (DPD), a particle-based method for mesoscopic simulations of complex fluid and soft matter systems. In DPD, each particle corresponds to a lump of atoms or molecules, where the particle motion is dictated by a pairwise force that is imposed between the DPD particles. A detailed description and validation of the DPD simulation method of RBCs in capillary and shear flows can be found in (12, 13).

Cell adhesion dynamics is a complex stochastic process, affected by cell shape, mechanical properties (*e.g.*, elasticity and bending rigidity) and flow conditions (*e.g.*, shear stress). In our previous studies, we have performed detailed computational simulations of cell adhesion dynamics to quantify the biophysical characteristics of malaria-infected RBCs in microcirculation (14, 15) and probe vaso-occlusion phenomena in SCD (16). Our results revealed that all these factors are important and especially the cell deformability and the strength of the bonds. In the present study, based on the experimental observations, we have documented that there is always a firm adhesion initially at one site, and this is what we impose in our simulations. This model is then used to examine the morphological and mechanical factors involved in cell adhesion dynamics of the sickle mature erythrocytes (SMEs) and the irreversible sickle cells (ISCs) once a strong initial attachment has been already formed (see Figs. 2-3 and Movie S2 and S8).

Sickle cell models. The membrane of SMEs and ISCs is modeled by a triangulated surface with 500 vertices. On the membrane surface, each respective vertex is represented by a DPD particle. The membrane elasticity of cells is imposed by viscoelastic bonds in-between the DPD particles. The cell bending rigidity is modeled by the bending resistance between the triangulated surfaces adjacent to each other. The incompressibility of the lipid bilayer and the cytosol are imposed by area and volume constraints. Sickle cells undergo a morphological transition from a normal biconcave shape to irregular and heterogeneous shapes, *e.g.* granular, elongated, and crescent (classic sickle) shapes, due to the polymerization of intracellular sickle hemoglobin (HbS) molecules. Due to the fact that it is computationally prohibitive to model polymerization at the molecular level in shear flow, we instead directly model the distortion of RBCs induced by the growing of HbS polymer fibers by applying “effective surface tension” on the cell membrane to transform a normal (AA) discocyte-shaped RBC into a sickle RBC, as we have done in (17). The shapes that we introduce in the simulations correspond to the shapes that we observe in the videos in the experiment (try to match). In previous work, we have developed a molecular-level mechanistic models to simulate the polymerization and the subsequent growth and branching processes of HbS (18, 19). We have also developed a kinetic cell sickling model to investigate the cell morphological sickling process under transient hypoxia (3). The kinetic model accounts for cell morphological change, cell sickling delay time, and cell membrane stiffening under transient hypoxia. For details on the sickle RBC models, we refer to refs. (3, 17, 20).

SMEs of low-density, high-deformability cells and are modeled to have deformable membrane even under hypoxia, consistent with previous findings (21, 22). Hence, we have modeled the SMEs with membrane mechanical properties similar to those of normal AA-RBCs, *i.e.*, shear modulus $\mu_0 = 4.7$ pN/ μm and bending rigidity $k_b = 2.4 \times 10^{-19}$ J. For ISCs in normoxia, the cell rigidity can be 2-3 orders of magnitude larger than the normal AA-RBCs (23). Here, we set the effective shear modulus of ISC to $100\mu_0$.

Adhesion dynamics. The adhesive interaction between the sickle RBC receptors and the ligand-coated substrate is modeled by the stochastic bond formation/dissociation (24–26). At each time step Δt , when the receptors on the cell membrane are close to ligands on the substrate within a characteristic length d_{on} , transient adhesive bonds can be formed with probability $P_{on} = 1 - e^{-k_{on}\Delta t}$, while the existing adhesive bonds can be ruptured with probability $P_{off} = 1 - e^{-k_{off}\Delta t}$ within a critical length d_{off} . The bond formation rate k_{on} and the bond dissociation rate k_{off} are defined by

$$k_{on} = k_{on}^0 \exp\left(-\frac{\sigma_{on}(l - l_0)^2}{2k_B T}\right) \quad [1]$$

$$k_{off} = k_{off}^0 \exp\left(\frac{\sigma_{off}(l - l_0)^2}{2k_B T}\right), \quad [2]$$

where σ_{on} and σ_{off} are the effective formation/rupture strengths. The unstressed reaction rates, k_{on}^0 and k_{off}^0 are molecular parameters of bond formation and bond dissociation kinetics, also called equilibrium rates or rate constants (27). For existing bonds, the force between the receptors and ligands is defined by $F(l) = 2k_s(l - l_0)$, where k_s is the spring constant, l is a separation distance between a receptor and a ligand and l_0 is the equilibrium length. We note that cell adhesion dynamics is

a protein-dependent process, and different receptor-ligand binding exhibits different adhesive characteristics. Even for the same or similar receptor-ligand bonds, bond dissociation kinetics may be regulated by several biophysical factors such as force history, contact duration, and approach velocity (28–30). For example, the equilibrium bond dissociation rate, k_{off}^0 , of the bond of P-selectin (*i.e.*, cell adhesion molecule on the surface of activated endothelial cells) and its primary ligand: the P-selectin glycoprotein ligand 1 (PSGL-1), is in the range of 10^{-2} – 10^1 s^{-1} at different unbinding force measurements obtained by using atomic force microscopy (AFM) (28–31). In this work, we chose a set of adhesive parameters for both SME and ISC models (14, 16, 25, 31–33) presented in Table S2.

Sensitivity analysis. We have performed extensive sensitivity studies for the adhesion dynamics of sickle cells by changing the equilibrium bond formation rate, k_{on}^0 . In Fig. 3C we model granular-shaped SMEs, whereas in Fig. S4A we model discoid-shaped SMEs. In both figures the modeled SMEs exhibit increasing numbers of adhesion binding sites with increasing bond formation rate k_{on}^0 .

As shown in Fig. S4A, discoid SMEs have increasing number of adhesion sites with increasing bond formation rate, which is similar to the adhesion dynamics of granular SMEs (Fig 3C). In Fig. S4B we compare modeled granular, discoid and elongated SME shapes at different values of the bond formation rate (0.1 – 10 k_{on}^0), while the cell-wall contact area is comparable in all modeled shapes. We observe that the number of adhesion sites per cell is less dependent on the cell shape, but it correlates rather strongly with increasing reaction rate, see Fig. S4B. Since the contact area of varying SME shapes is comparable, bond formation rate becomes a dominant factor in their adhesive dynamics. For ISCs, however, the number of adhesion sites fluctuates between 1 and 2 when the equilibrium bond formation rate is within the range of 0.1 – 10 k_{on}^0 , indicating that it is more difficult for the ISCs to form adhesive binding sites (16).

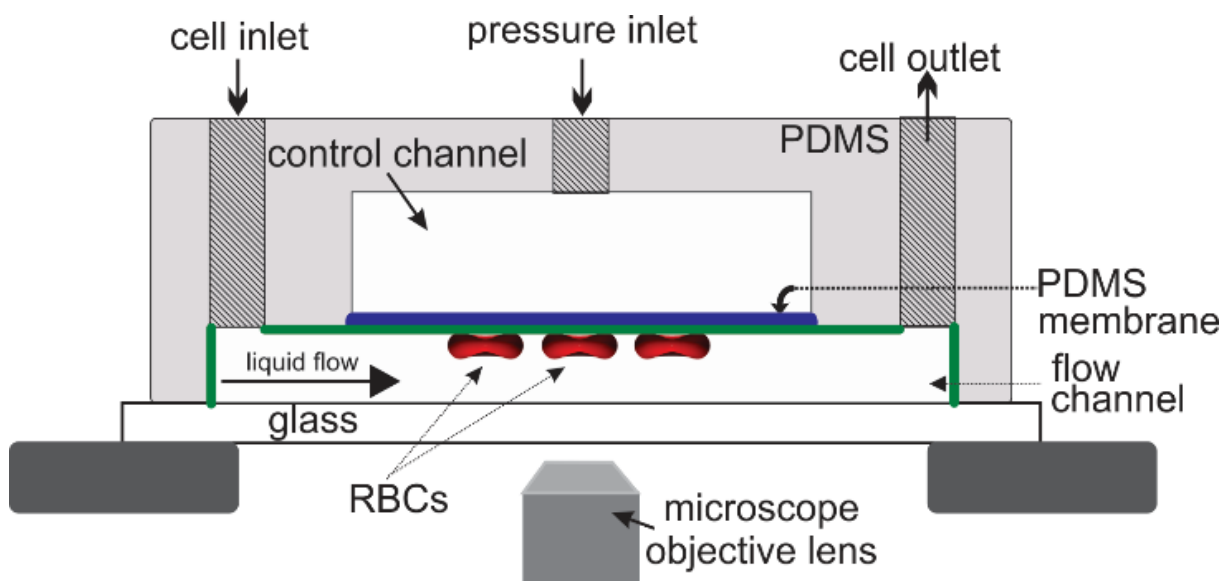


Fig. S1. Cross-sectional schematic representation of the sickle cell adhesive dynamics microfluidic device: The dual-layer design consists of a "flow channel" *i.e.*, flow of RBC suspension and a "gas channel" for gas mixture and pressure regulation. Representative RBC adherent cell (in red) under a microscope's objective lens field of view. Gas-permeable PDMS membrane in blue. FN-functionalized surfaces in green. Precise liquid flow profile can be delivered through a pressure differential from the "cell inlet and outlet". (Schematic not in scale).

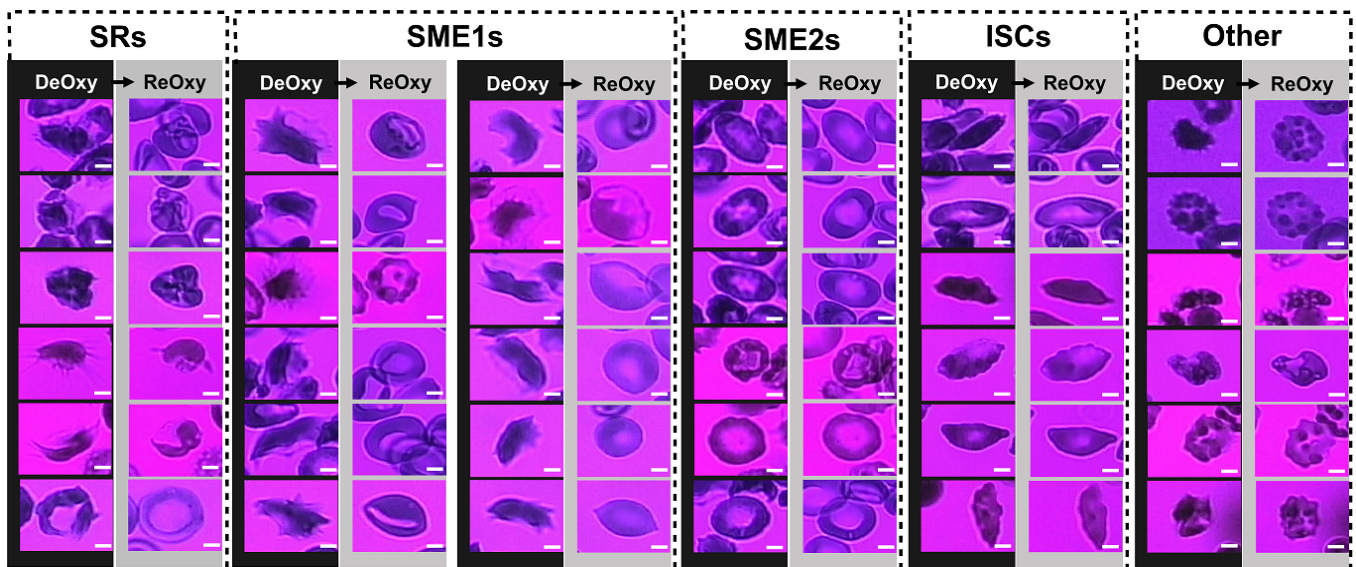


Fig. S2. Adherent sickle cell classification, in hypoxia (black background) and subsequent reoxygenation (grey background). Sickle Reticulocytes in circulation (SRs): SRs can either have a multi lobular morphology or an asymmetric "deep dish" morphology. Class I sickle mature erythrocytes (SME1): SME1s exhibit significant morphological shape change under hypoxia; in normoxia SME1s are mostly discoid sickle cells and have smooth surface contours. Class II mature sickle cells (SME2): SME2s largely maintain their normoxia shape even under hypoxia with irregular surface contour; in normoxia SME2s are mostly elliptocytic sickle cells with already slightly irregular surface contours. Irreversibly Sickled Cells (ISCs): ISCs have elongated and elliptocytic morphology in addition to irregular surface contours in normoxia. Other: Cells of mostly echinocyte-type and odd-shaped cells that do not fall into any of the previous categories. Wall shear stress range 0.03 - 0.08 Pa. FN-coated microchannel wall. Scale bar: 2.5 μm .

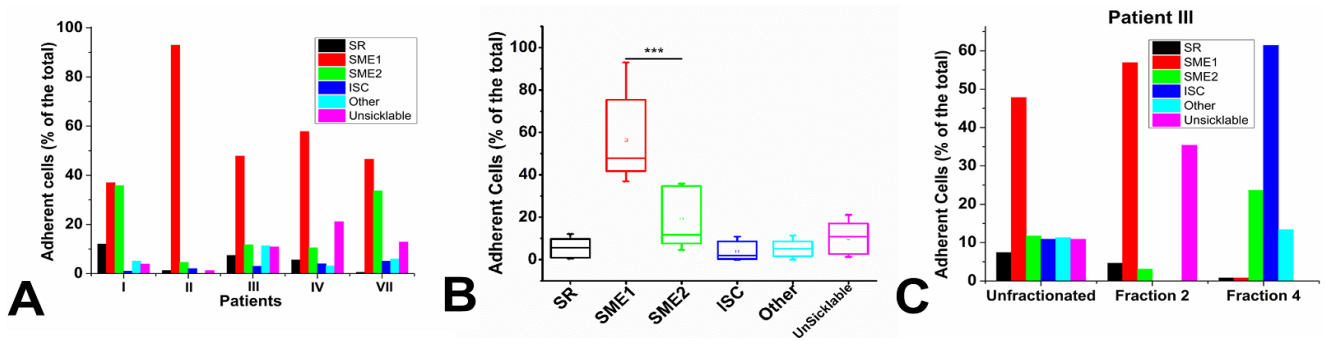


Fig. S3. Adherent cell classification statistics. (A) Non-fractionated cell density data. Adherent cells (% of the total cells per sample) for Patients I, II, III, IV and VIII as identified in Table S1). (B) Non-fractionated cell density data. Box plot of adherent cells (% of the total cells per sample) for Patients I, II, III, IV and VIII (Table S1). Standard analysis of variance tests were used to determine the significance of the means difference between the adherent cell categories, where $***P < 0.001$. Horizontal lines within the boxes represent the mean value within the distribution, whereas the vertical bars represent the Min and Max values. (C) Density-fractionated cell data. Adherent cells (% of the total cells per sample) for Patient III (Table S1)

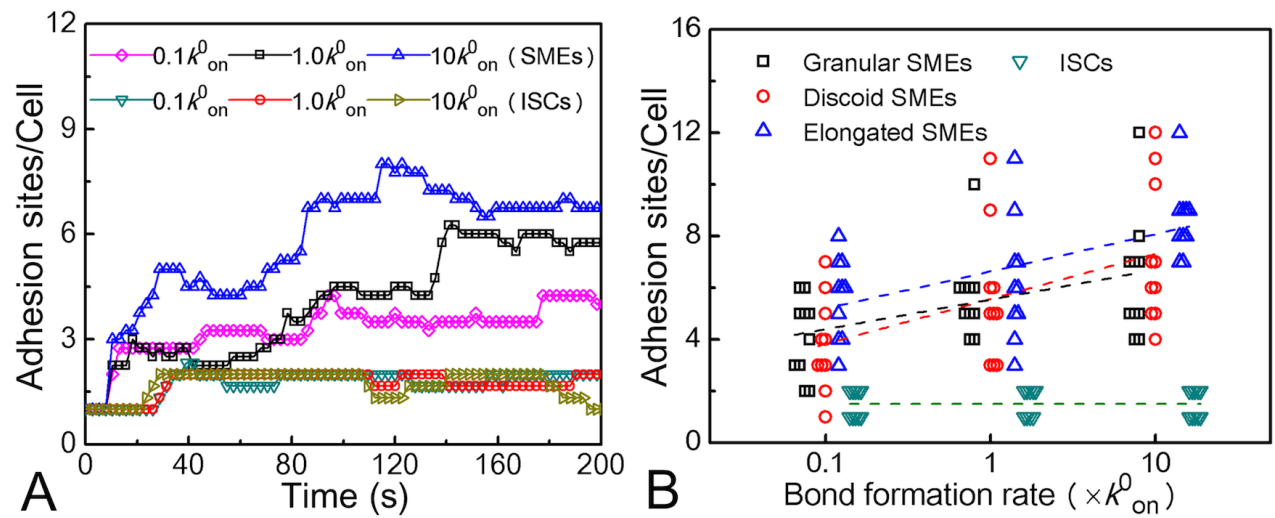


Fig. S4. Sensitivity studies via simulations. (A) Average number of adhesion sites/cell (N_a) as a function of time for discoid SMEs and ISC at different bond formation rates, where k_{on}^0 is the rate constant. (B) The number of adhesion sites/cell of SMEs and ISCs ($t=150$ s) at different bond formation rates. Overlapped data is shifted horizontally for clarity and the dashed lines show linear fitting of N_a of different sickle cell models.

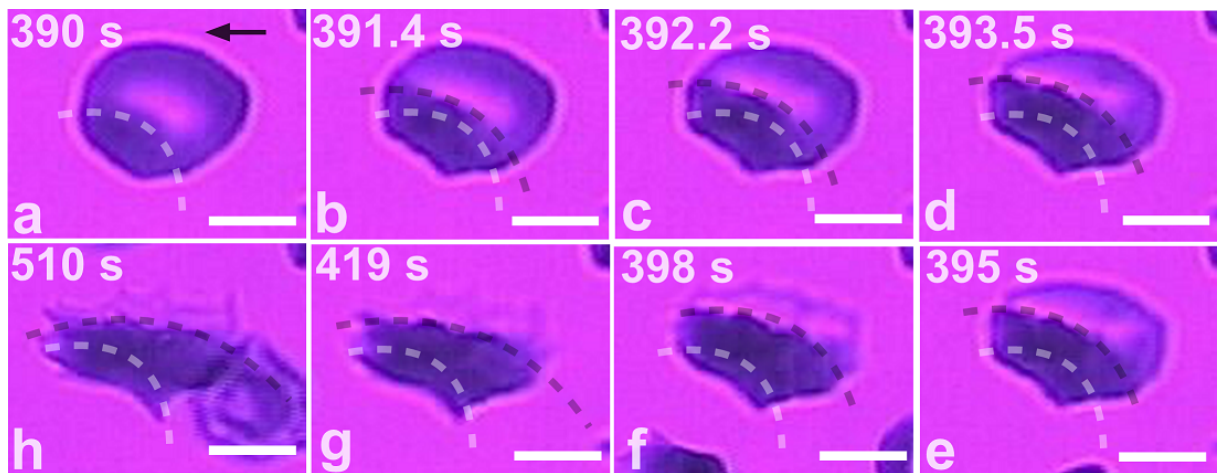


Fig. S5. Snapshots of the movement of the "polymerized front" in transitional SME (cell in Fig. 4B), under hypoxia and shear flow. (a) Cell morphology at the onset of transition (identical to Fig. 4B, b). White dotted line in all snapshots is the starting position of the front as a reference. Black dotted line shows the front progression. (h) Final hypoxia-shape. The cell attains its hypoxia-shape and underlying adhesion sites are revealed. Wall shear stress 0.08 Pa. Black arrow denotes the flow direction. Scale bars: 5 μm . Area of FOV: $\sim 255 \mu\text{m}^2$.

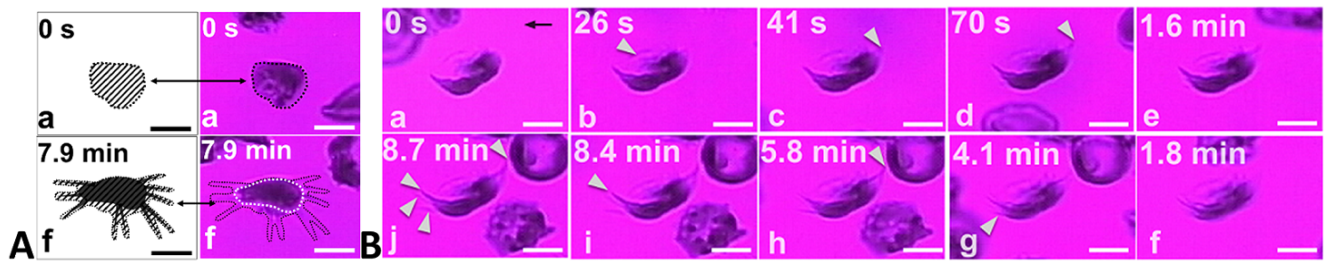


Fig. S6. (A) Cell-wall contact area of the SR of Fig. 5. Hatched area roughly represents the contact area of the cell's lipid bilayer. Hatched area in f. ($t = 7.9$ min) is approximately two times larger than the hatched area in a. ($t = 0$). (B) Snapshots of simultaneous adhesion and polymerization in SR under hypoxia and shear flow (cell "a" in Fig. 1A). ($t = 0$) The cell adheres on the surface. ($t = 26$ s) Initiation of gradual protrusion of polymer fibers (white pointers). (4.1 min $< t < 8.4$ min) HbS polymer projections grow from opposing ends of the adherent cell. ($t = 8.7$ min) Previously noted HbS polymer projections continue to grow, stretching the cell outwards. Black arrow denotes the flow direction. Wall shear stress 0.05 Pa. FN-coated microchannel wall. Scale bar: $5 \mu\text{m}$. Area of FOV: $\sim 330 \mu\text{m}^2$.

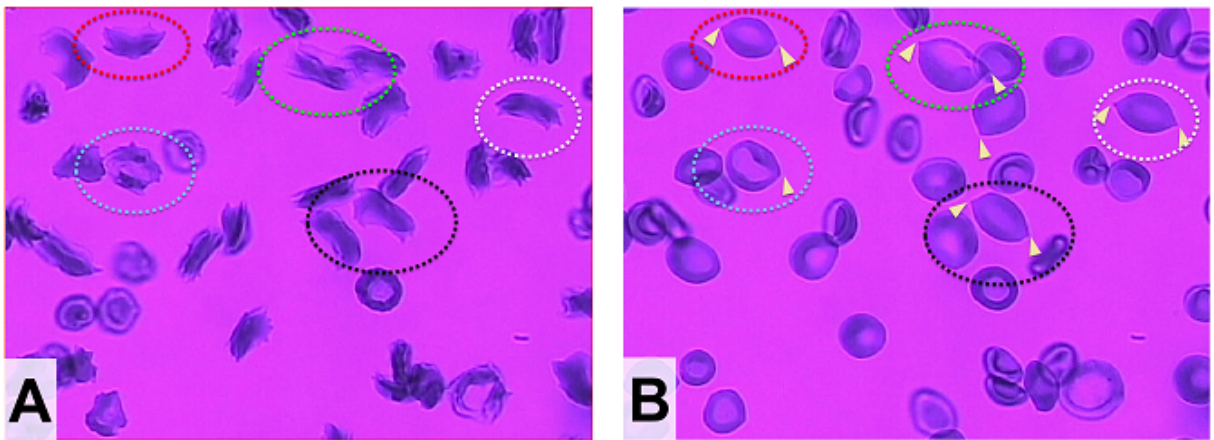


Fig. S7. Residual post-hypoxia adhesion sites. (A) Hypoxia: Snapshot of adherent sickle cells after ~ 10 min of shear flow under hypoxia. (B) Reoxygenation: Adherent sickle cells after 2 min of reoxygenation; yellow pointers indicate the post-hypoxia residual adhesion sites. Ovals of the same color correspond to identical cells before and after reoxygenation (also see [Movie S7](#)).

Table S1. Clinical Measurements

	Genotype	WBC	HCT	MCV, fl	MCHC, g/dl	On-Hydroxyurea	HbS, %	HbF, %	HbA, %	HbA2, %
Patient I	HbSS	12.8	29.2	93.1	33.6	N	65.4	20.1	0	3.2
Patient II	HbSS	6.2	42.2	76	33.6	N	N/A	N/A	N/A	N/A
Patient III	HbSS	17.5	16.4	70.4	36	N	73	20.60	2.9	3.5
Patient IV	HbSS	8.71	23.9	131.3	35.6	Y	81.80	11.80	2.30	4.10
Patient V	HbSS	N/A	N/A	N/A	N/A	N	88.2	3.8	0	4.1
Patient VI	HbSS	N/A	N/A	N/A	N/A	N	94.2	2.5	0	3.3
Patient VII	HbSS	10.4	20.7	96.7	34.2	N	N/A	7.4	N/A	N/A
Patient VIII	HbSS	11.6	25.2	66.5	32.7	N	82.3	8.1	2.6	7

Complete blood count (CBC) analysis results provided the white blood count (WBC), hematocrit (HCT), mean corpuscular volume (MCV) and mean corpuscular hemoglobin concentration (MCHC). Gel electrophoresis is used to identify the fraction (%) of HbS, hbF, HbA and HbA2 of each patient sample.

Table S2. Simulation (in DPD units) and physical (in SI units) parameters for SME and ISC adhesion dynamics

Parameters	Simulations	Physical	Ref.
Spring constant (k_s)	400	1.84×10^{-4} N/m	(14, 25)
Equilibrium spring length (l_0)	0.0	0.0 μm	(16, 33)
Reaction distance (d_{on})	0.05	0.05 μm	(14, 16)
Rupture distance (d_{off})	0.35	0.35 μm	(14)
On strength ($\sigma_{on}/k_B T$)	10.58	10.58 μm^{-2}	(16)
Off strength ($\sigma_{off}/k_B T$)	3.49	3.49 μm^{-2}	(16)
Unstressed on rate (k_{on}^0)	10	115 s^{-1}	(32)
Unstressed off rate (k_{off}^0)	0.001	0.0115 s^{-1}	(31)

Movie S1. Morphological heterogeneity of adherent sickle cells to FN-coated microchannel wall under hypoxia and shear flow for ~ 10 min. Wall shear stress 0.05 Pa. Area of FOV: $\sim 5,766 \mu\text{m}^2$. (Movie is sped up 20x)

Movie S2. SME adherence onset in slow motion. Cell "g" of Fig. 1A. The cell forms a pointed membrane edge and then flips around the adhesion site to align with the flow direction. Wall shear stress 0.05 Pa. (Movie is slowed down 4x)

Movie S3. SME simultaneous adhesion and polymerization; from single-site to multiple-site adhesion. Cell "g" of Fig. 1A. Following initial attachment and alignment with the flow, the cell exhibits an oscillatory motion under shear flow, indicative of a single initial adhesion site. After ~ 2 min, the oscillation ceases and the cell appears firmly in place, which is a clear indication of the development of multiple adhesion sites while adherent. Wall shear stress 0.05 Pa. (Movie is sped up 10x)

Movie S4. Simulation of adhesion dynamics of an SME under shear flow (Fig. 2). Green dots in the background matrix represent an array of ligands that simulate a FN-coated adhesion surface. Initially the cell has only one adhesion site then additional adhesion sites are formed over time. Wall shear stress 0.04 Pa.

Movie S5. SR simultaneous adhesion and polymerization. Cell "b" of Fig. 1A. Movie shows multiple HbS polymer fibers grow from the cell bulk irrespectively of the flow direction. The cell stretches in different directions on the surface, driven by the outward growth of fibers. Wall shear stress 0.05 Pa. (Movie is sped up 20x)

Movie S6. Adhesion favors polymerization in sickle RBCs. Adhesion prolongs the residence time of SMEs in hypoxia prior to the morphological sickling event, while sickling occurs spontaneously and not gradually. After ~ 7 min adherent, the cells attain their hypoxia-shape and underlying adhesion sites are revealed. (Movie is sped up 20x)

Movie S7. Reoxygenation movie of Fig. S7: Adherent cells following reoxygenation do not detach from the surface. Yellow pointers indicate post-hypoxia residual adhesion sites. Wall shear stress 0.08 Pa. (Movie is sped up 2x)

Movie S8. ISC simultaneous adhesion and polymerization close-up. Cell "m" of Fig. 1A. The cell adheres to the surface and flips around the adhesion site aligning with the flow direction. Following that, the cell oscillates due to shear flow. Wall shear stress 0.05 Pa. (Movie is sped up 20x)

Movie S9. Simulation of adhesion dynamics of an ISC under shear flow (Fig. 3). Green dots in the background matrix represent an array of ligands that simulate a FN-coated adhesion surface. The total number of adhesion sites for ISCs is fewer compared to those for SMEs.

Movie S10. SR reoxygenation close-up. Cell "b" of Fig. 1A. During this hypoxia-to-reoxygenation cycle the polymerized HbS fibers that protrude from the initial cell boundary retract into the cell upon reoxygenation. Post-hypoxia projections indicate residual adhesion sites. (Movie is sped up 3x)

Movie S11. SR reoxygenation close-up. Cell "a" of Fig. 1A. The polymerized HbS fibers that protrude from the initial cell boundary retract into the cell upon reoxygenation. (Movie is sped up 3x)

Movie S12. SR reoxygenation close-up of Fig. 6C. Reoxygenation shows that the SR fully recovers the "deep-dish" morphology. In normoxia, granules are visible within the refractile ring. (Movie is sped up 2x)

References

1. Hosseini P, et al. (2016) Cellular normoxic biophysical markers of hydroxyurea treatment in sickle cell disease. *Proceedings of the National Academy of Sciences* p. 201610435.
2. Du E, Diez-Silva M, Kato GJ, Dao M, Suresh S (2015) Kinetics of sickle cell biorheology and implications for painful vasocclusive crisis. *Proceedings of the National Academy of Sciences* 112(5):1422–1427.
3. Li X, Du E, Dao M, Suresh S, Karniadakis GE (2017) Patient-specific modeling of individual sickle cell behavior under transient hypoxia. *PLOS Comput. Biol.* 13:e1005426.
4. Chasis JA, Prenant M, Leung A, Mohandas N (1989) Membrane assembly and remodeling during reticulocyte maturation. *Blood* 74(3):1112–1120.
5. Mel HC, Prenant M, Mohandas N (1977) Reticulocyte motility and form: studies on maturation and classification. *Blood* 49(6):1001–1009.

6. Coulombel L, Tchernia G, Mohandas N (1979) Human reticulocyte maturation and its relevance to erythropoietic stress. *The Journal of laboratory and clinical medicine* 94(3):467–474.
7. Mohandas N, Evans E (1985) Sickle erythrocyte adherence to vascular endothelium. morphologic correlates and the requirement for divalent cations and collagen-binding plasma proteins. *Journal of Clinical Investigation* 76(4):1605.
8. Kaul DK, Fabry M, Windisch P, Baez S, Nagel R (1983) Erythrocytes in sickle cell anemia are heterogeneous in their rheological and hemodynamic characteristics. *Journal of clinical investigation* 72(1):22.
9. Bessis M, Bricka M (1952) Aspect dynamique des cellules du sang. son étude par la microcinématographie en contraste de phase. *Rev Hematol* 7(3):407–435.
10. Xu M, et al. (2017) A deep convolutional neural network for classification of red blood cells in sickle cell anemia. *PLoS Computational Biology* 13(10):e1005746.
11. Mohandas N, Evans E (1984) Adherence of sickle erythrocytes to vascular endothelial cells: requirement for both cell membrane changes and plasma factors. *Blood* 64(1):282–287.
12. Pivkin IV, Karniadakis GE (2008) Accurate coarse-grained modeling of red blood cells. *Phys. Rev. Lett.* 101(11):118105.
13. Fedosov DA, Caswell B, Karniadakis GE (2010) A multiscale red blood cell model with accurate mechanics, rheology, and dynamics. *Biophys. J.* 98(10):2215–2225.
14. Fedosov DA, Caswell B, Karniadakis GE (2011) Wall shear stress-based model for adhesive dynamics of red blood cells in malaria. *Biophysical journal* 100(9):2084–2093.
15. Fedosov D, Caswell B, Suresh S, Karniadakis G (2011) Quantifying the biophysical characteristics of plasmodium-falciparum-parasitized red blood cells in microcirculation. *Proceedings of the National Academy of Sciences* 108(1):35–39.
16. Lei H, Karniadakis GE (2013) Probing vasoocclusion phenomena in sickle cell anemia via mesoscopic simulations. *Proc. Natl. Acad. Sci. U.S.A.* 110(28):11326–11330.
17. Lei H, Karniadakis GE (2012) Quantifying the rheological and hemodynamic characteristics of sickle cell anemia. *Biophysical journal* 102(2):185–194.
18. Lu L, Li X, Vekilov PG, Karniadakis GE (2016) Probing the twisted structure of sickle hemoglobin fibers via particle simulations. *Biophysical journal* 110(9):2085–2093.
19. Lu L, Li H, Bian X, Li X, Karniadakis GE (2017) Mesoscopic adaptive resolution scheme toward understanding of interactions between sickle cell fibers. *Biophysical Journal* 113(1):48–59.
20. Lei H, Karniadakis GE (2012) Predicting the morphology of sickle red blood cells using coarse-grained models of intracellular aligned hemoglobin polymers. *Soft Matter* 8(16):4507–4516.
21. Kaul DK, Chen D, Zhan J (1994) Adhesion of sickle cells to vascular endothelium is critically dependent on changes in density and shape of the cells. *Blood* 83(10):3006–3017.
22. Kaul DK, Fabry ME, Nagel RL (1989) Microvascular sites and characteristics of sickle cell adhesion to vascular endothelium in shear flow conditions: pathophysiological implications. *Proceedings of the National Academy of Sciences* 86(9):3356–3360.
23. Itoh T, Chien S, Usami S (1995) Effects of hemoglobin concentration on deformability of individual sickle cells after deoxygenation. *Blood* 85(8):2245–2253.
24. Bell GI, et al. (1978) Models for the specific adhesion of cells to cells. *Science* 200(4342):618–627.
25. Hammer DA, Apte SM (1992) Simulation of cell rolling and adhesion on surfaces in shear flow: general results and analysis of selectin-mediated neutrophil adhesion. *Biophysical journal* 63(1):35–57.
26. King MR, Hammer DA (2001) Multiparticle adhesive dynamics: hydrodynamic recruitment of rolling leukocytes. *Proceedings of the National Academy of Sciences* 98(26):14919–14924.
27. Ley K (2009) *Leucocyte Adhesion*, Current Topics in Membranes. (Elsevier Science).
28. Zhang Y, Sun G, Lü S, Li N, Long M (2008) Low spring constant regulates p-selectin-psgl-1 bond rupture. *Biophysical journal* 95(11):5439–5448.
29. Lü S, Ye Z, Zhu C, Long M (2006) Quantifying the effects of contact duration, loading rate, and approach velocity on p-selectin–psgl-1 interactions using afm. *Polymer* 47(7):2539–2547.
30. Marshall BT, Sarangapani KK, Lou J, McEver RP, Zhu C (2005) Force history dependence of receptor-ligand dissociation. *Biophysical journal* 88(2):1458–1466.
31. Fritz J, Katopodis AG, Kolbinger F, Anselmetti D (1998) Force-mediated kinetics of single p-selectin/ligand complexes observed by atomic force microscopy. *Proceedings of the National Academy of Sciences* 95(21):12283–12288.
32. Gupta V, Eggleton C (2012) A theoretical method to determine unstressed off-rate from multiple bond force spectroscopy. *Colloids and Surfaces B: Biointerfaces* 95:50–56.
33. Pierres A, Benoliel AM, Bongrand P (1998) Studying receptor-mediated cell adhesion at the single molecule level. *Cell adhesion and communication* 5(5):375–395.